Stem Cell Research (2010) 5, 201–211

available at www.sciencedirect.com

ScienceDirect

www.elsevier.com/locate/scr

REGULAR ARTICLE

Semiquantitative histopathology and 3D magnetic resonance microscopy as collaborative platforms for tissue identification and comparison within teratomas derived from pedigreed primate embryonic stem cells

Carlos A. Castro [a,b,1], Ahmi Ben-Yehudah [a,b,1], John A. Ozolek [c,1], Parker H. Mills [d,1], Carrie J. Redinger [a], Jocelyn D. Mich-Basso [a], David A. McFarland [a], Stacie L. Oliver [a], Eric T. Ahrens [d], Gerald Schatten [a,b,e,*]

[a] *Pittsburgh Development Center, University of Pittsburgh School of Medicine, Pittsburgh, PA, USA*
[b] *Department of Ob/Gyn and Reproductive Sciences, University of Pittsburgh School of Medicine, Pittsburgh, PA, USA*
[c] *Department of Pathology, Children's Hospital of Pittsburgh, University of Pittsburgh School of Medicine, Pittsburgh, PA, USA*
[d] *Department of Biological Sciences and Pittsburgh NMR Center for Biomedical Research, Carnegie Mellon University, Pittsburgh, PA, USA*
[e] *Department of Cell Biology and Physiology and Bioengineering, University of Pittsburgh School of Medicine, Pittsburgh, PA, USA*

Received 24 May 2010; received in revised form 28 July 2010; accepted 29 July 2010

Abstract Teratoma formation in xenografts is a sufficiently stringent pluripotency assay for stem cells. However, little is known about the composition and spatial relationships of tissues within teratomas that may provide clues about development and platforms for studying organ development. Additionally, teratoma formation and analysis lack standards for reporting as assays of pluripotency. Three of 27 total teratomas derived from pedigreed primate embryonic stem cells underwent quantitative three-dimensional high-resolution magnetic resonance microscopy (MRM). Teratomas were subsequently serially sectioned and tissue types identified, semiquantitated, and correlated with MRM images. All teratomas demonstrated tissue derivatives from the three germ layers and approximately 23 different tissue types were identified. Certain tissue groups attempted to form organs more frequently (e.g., trachea/bronchi, small intestine). MRM discriminated some tissues readily (e.g., bone, adipose, cartilage) while other tissue types with like MR intensities could not be distinguished. Semiquantitative histopathological analysis of teratomas demonstrates the ability to delineate multiple tissues as derived from ectoderm,

* Corresponding author. Magee Womens Research Institute, 204 Craft Avenue, Pittsburgh, PA 15213, USA. Fax: +1 412 641 2410.
E-mail addresses: ccastro@mwri.magee.edu (C.A. Castro), abenyehudah@mwri.magee.edu (A. Ben-Yehudah), ozolekja@upmc.edu (J.A. Ozolek), phm@andrew.cmu.edu (P.H. Mills), credinger@mwri.magee.edu (C.J. Redinger), jdm114@pitt.edu (J.D. Mich-Basso), dmcfarland@mwri.magee.edu (D.A. McFarland), soliver@mwri.magee.edu (S.L. Oliver), eta@andrew.cmu.edu (E.T. Ahrens), schattengp@upmc.edu (G. Schatten).
[1] These authors contributed equally.

1873-5061/$ – see front matter
doi:10.1016/j.scr.2010.07.005

mesoderm, or endoderm and to use this information for comparison to other teratomas. MRM provides rapid quantitative imaging of intact teratomas that complements histology and identifies sites of interest for additional biological studies.

Introduction

Embryonic stem cells (ESCs) are defined by their ability to self-renew and differentiate (Mountford, 2008). They are characterized by their expression of specific markers (SSEA-3/4, TRA, Oct4, Nanog, and others) (Hyun et al., 2008) and their behavior in cell culture (differentiation into all three germ layers). One of the stringent criteria for ESC lines derived from human and nonhuman primates is their ability to produce a teratoma tumor when injected into immunocompromised mice (Lanza, 2006). Additional stem cell types have also been shown to produce teratomas including certain germline stem cells and induced pluripotent stem cells (iPSC) (Aleckovic and Simon, 2008). Other purported pluripotent cells such as human embryonic and primordial germ cells and amnion-derived cells have demonstrated *in vitro* multilineage potential but have not shown teratoma formation *in vivo*. A teratoma is a tumor strictly defined in pathological terms by histological evidence of tissue types contributed by each of the original three germ layers including ectoderm (e.g., neuroepithelium, mature neuroglial tissue, skin), mesoderm (e.g., smooth and skeletal muscle, connective tissue, bone, and cartilage), and endoderm (e.g., lung and intestinal mucosa, pancreas, liver) (Sternberg, 1989).

While at first glance, most teratomas appear as disorganized masses with recognizable tissue types contributed from the three basic germ layers and even focal organogenesis, little is known about the contribution of each germ layer to the lesion and this information may hold important clues to normal and abnormal development (Aleckovic and Simon, 2008; Damjanov, 1993; Lehman, 1980; Lehtonen et al., 1989; Prelle et al., 2002). Studying the cellular and tissue milieu within teratomas both *in vivo* and *ex vivo* would help in beginning to answer the following questions: How much of each specific tissue type is present? Do the tissues present recapitulate normal development spatiotemporally? How are the tissues present affected in type and quantity when derived from ESCs that have been manipulated genetically (induced chromosomal aberration, addition/deletion of specific genes) and environmentally (that is, by drugs or toxins, nutrients)? Do all ESC lines have the equal potential of differentiating successfully into a specific cell type that could be potentially used to treat specific diseases such as diabetes or Parkinson disease? Because many of these questions may begin to be addressed with more rigorous examination of teratomas derived from ESCs, a recent call to standardize the reporting criteria for teratomas derived from ESCs and iPS cells has been proposed by Muller et al. (2010). Their report underscored the lack of standards for the production of teratomas, lack of reporting teratoma formation, and the lack of consistency in reporting teratoma results within publications using or deriving human ESCs or iPSCs.

With this in mind, the aim was systematic evaluation and careful comparison of teratomas derived from pedigreed primate embryonic stem cells (nhpESCs) using two distinctive modalities: magnetic resonance microscopy (MRM), a high-resolution relative of magnetic resonance imaging (MRI), and conventional semiquantitative histopathology. As clinical MR image quality and resolution continue to improve, the use of MRI in studies using embryonic stem cells transplantation will allow for imaging of cellular trafficking and tissue/organ development. Ensuring embryonic cell transplantation safety by noninvasive detection and monitoring of atypical cellular behaviors is also a pressing need (Cao et al., 2009). In anticipation of these developments, we studied high-resolution MR images of teratomas derived from nhpESCs and correlated these MR images with careful and semiquantitative histopathology. No previous studies report *ex vivo* MRM of teratomas, or attempt to correlate teratoma MR images with histology.

We found that teratomas can be derived from injection of immunodeficient mice with a high success rate using pedigreed nhpESCs. Teratomas exhibited a broad range of tissue amounts and tissue types derived from all germ layers including yolk sac elements. MRM is a noninvasive *in vivo* and *ex vivo* means to evaluate teratoma tissue content, tissue volume data, and reliably identify specific tissue types for longitudinal follow-up.

Results

Since derived pedigreed nonhuman primate ESCs were injected into mice to identify their pluripotency by ability to form teratomas, we could utilize them for more detailed analysis and comparison of tissue morphology and distribution within each teratoma and between teratomas using histopathology and MRM.

Overall, no statistical differences were found for number of blocks needed (crude estimate of size) when comparing all teratomas between families and when comparing all teratomas by gender. Eight teratomas were derived out of 12 injections (67% success) from 3 lines within one family, compared to 19 teratomas derived from 22 injections (86% success) of 4 lines in the other family. Two injections (106-A1, A2) resulted in a moderate to poorly differentiated tumor (see below) without evidence of teratoma formation. Two injections from another line (306-C1, C2) produced a dermoid cyst on one side (left testis) and no detectable lesion from the other injection (right testis) (not shown). Two injections did not produce a detectable lesion and one produced a lesion with only two germ layers represented. Table 1 shows characteristics of the three teratomas that also underwent MRM.

We next compared in a semiquantitative fashion, the relative contributions of each germ layer to the composition of each teratoma using the scale provided under Methods. Table 1 also demonstrates the median contributions of each germ layer for each teratoma for which MRM was performed.

Table 1 Demographic and germ layer scores for teratomas derived from pedigreed primate ESCs for which MRM was performed

	3006-C1	3006-C2	3106-B1
Gender	F	F	M
Incubation time (days)	98	98	106
No. blocks/lesion	7	12	7
Ectoderm [a]	1	1	4
Mesoderm	5	3	1
Endoderm	1	1	1

[a] Scoring for percentage of germ layer tissues present: 1, 1-20%; 2, 21-40%; 3, 41-60%; 4, 61-80%; 5, 81-100%.

For these teratomas, wide discrepancies were found in tissue type quantity with wide variations in ectodermal versus mesodermal derivatives. However, in the overall analysis of the teratomas, no differences were noted between families for median contribution of germ layers or between sexes either within families or between families.

Overall, approximately 23 different tissue types were identified as derivatives of ectoderm (Figs. 1A–E), mesoderm (Figs. 1F–O), and endoderm (Figs. 1P–T). Specific tissues seen infrequently are shown in Figures 1U–Y.

Ectodermal derivatives included immature neuroglial tissue represented by either neuroepithelial tissue composed of stratified elongated cells with hyperchromatic oval nuclei and pink cytoplasm arranged in ribbons and rosettes (Flexner-Wintersteiner and Homer Wright) (A) or adjacent cellular neuroglial tissue composed notably of small cells with scant cytoplasm resembling neuroblasts (B). Cells with granular brown pigment resembling retinal cells arranged in rosettes were seen sporadically and in low quantity in some teratomas associated with immature neural areas (B). Mature neuroglial tissue was defined as tissue containing mature neurons, glial cells, and background mature neuropil resembling disorganized brain or areas with well-developed ganglion (C, D). Skin was also present and in most cases demonstrated a well-developed epidermis and adnexal structures including in some cases hair follicles (E).

Mesodermal derivatives comprised the largest percentage of tissues overall in these teratomas and consisted of muscle (skeletal and smooth), fat, mesenchyme, cartilage, and bone (F–O). Smooth muscle showed a consistent morphology typical of mature smooth muscle found in the muscle layers of the gastrointestinal tract. Well-defined and recognizable smooth muscle was associated with glandular epithelium in most cases and rarely seen in isolation arising from the mesenchymal stroma. Often smooth muscle bundles were found in layers recapitulating the two distinct layers seen in the gastrointestinal tract of nonhuman primates, humans, and other mammals. In other areas where more primitive glandular epithelium was present, the surrounding stroma had the appearance of immature smooth muscle (G). Immature skeletal muscle (H) was delineated by multinucleated myotubes, immature myofibers, and single rhabdomyoblastic cells interspersed in cellular mesenchymal stroma. Mature skeletal muscle was apparent by long eosinophilic myofibers showing striations (I). Skeletal muscle comprised a large portion of the mesodermal component of teratoma from the 3106 line (J). Immature and mature adipose tissue was seen (K, L). The majority of adipose tissue was composed of lobules of mature adipocytes with focal areas of immature fat characterized by variation in size of adipocytes and the presence of lipoblasts. Undifferentiated stroma demonstrated several morphological variants including cellular spindle cell stroma with early collagenization (M), fibromuscular (N), mixed collagenous/myxoid stroma, and densely fibrotic (not shown). Within cellular areas numerous mitotic figures could be readily identified, although atypical nuclear structures or other malignant features were not seen. Bone and cartilage were frequently present in many teratomas (O). Cartilage displayed a range of morphology from cellular immature cartilage generally associated with neuroglial regions to more mature well-formed lobules of cartilage, some forming structures resembling tracheal rings (see Fig. 2S).

Endodermal derivatives exhibited no specific morphology, but had epithelium that generally lined cystic or glandular spaces (structures having a lumen, not neuroepithelial) (P–T). The epithelium varied considerably and included immature foveolar/intestinal type (P), primitive glandular (Q, R), stratified (S), and primitive endodermal (yolk sac) type (T). Ciliated and well-developed intestinal-type epithelium was also present in some teratomas. Conspicuously missing from all teratomas examined was evidence of well-developed thyroid, liver, kidney, or pancreas.

Both injections of line 106 (A1, A2) resulted in tumors with similar morphology best characterized as moderately to poorly differentiated tumor (Figs. 2A–C) shown here to illustrate one of the nonteratomatous lesions resulting from ESC injections. These tumors exhibited both focal areas of solid growth and areas of glandular differentiation. Interestingly, most of the tumor cells exhibited a mixed epithelial and mesenchymal phenotype by expression of cytokeratin and vimentin (Figs. 2D and E, respectively). Scattered periglandular cells demonstrated an immunophenotype reminiscent of myoepithelial cells including expression of smooth muscle actin, all muscle actin, and S100, respectively (Figs. 2F, G, and H). These periglandular cells were also negative for p63, a marker of basal cells in the sinonasal tract, breast, and prostate. Tumor cells were negative for PGP9.5, myogenin, and alpha-fetoprotein, making neuroblastic, skeletal muscle, or endodermal differentiation less likely. Oct-4 (pluripotency marker) and p63 (epithelial progenitor marker and marker of basal cells) did not show characteristic nuclear staining in any tumor cells. Three lines from 306 also formed undifferentiated/poorly differentiated tumors, but exhibited abnormal karyotypes in the derived lines.

As histopathological and immunohistochemistry analyses require removal of the teratoma from the mouse, we examined if we could utilize a noninvasive technique, i.e., MRM, for teratoma analysis. We performed MRM on two teratomas from line 3006 and an additional teratoma from line 3106. Figure 3 shows volumetric measurements and 3D volume renderings of each teratoma made from MRM images. Corresponding numerical measurements are shown in Supplemental Table 1. All three teratomas had measured volumes between 3.0 and 6.2 cc. A cystic volume fraction, ranging between 1 and 3%, was found only in teratomas from line 3006. In agreement with previous T_2-weighted MRI of teratomas, all cysts were high intensity and solid tissue had heterogeneous contrast (Yamaoka et al., 2003; Monteiro

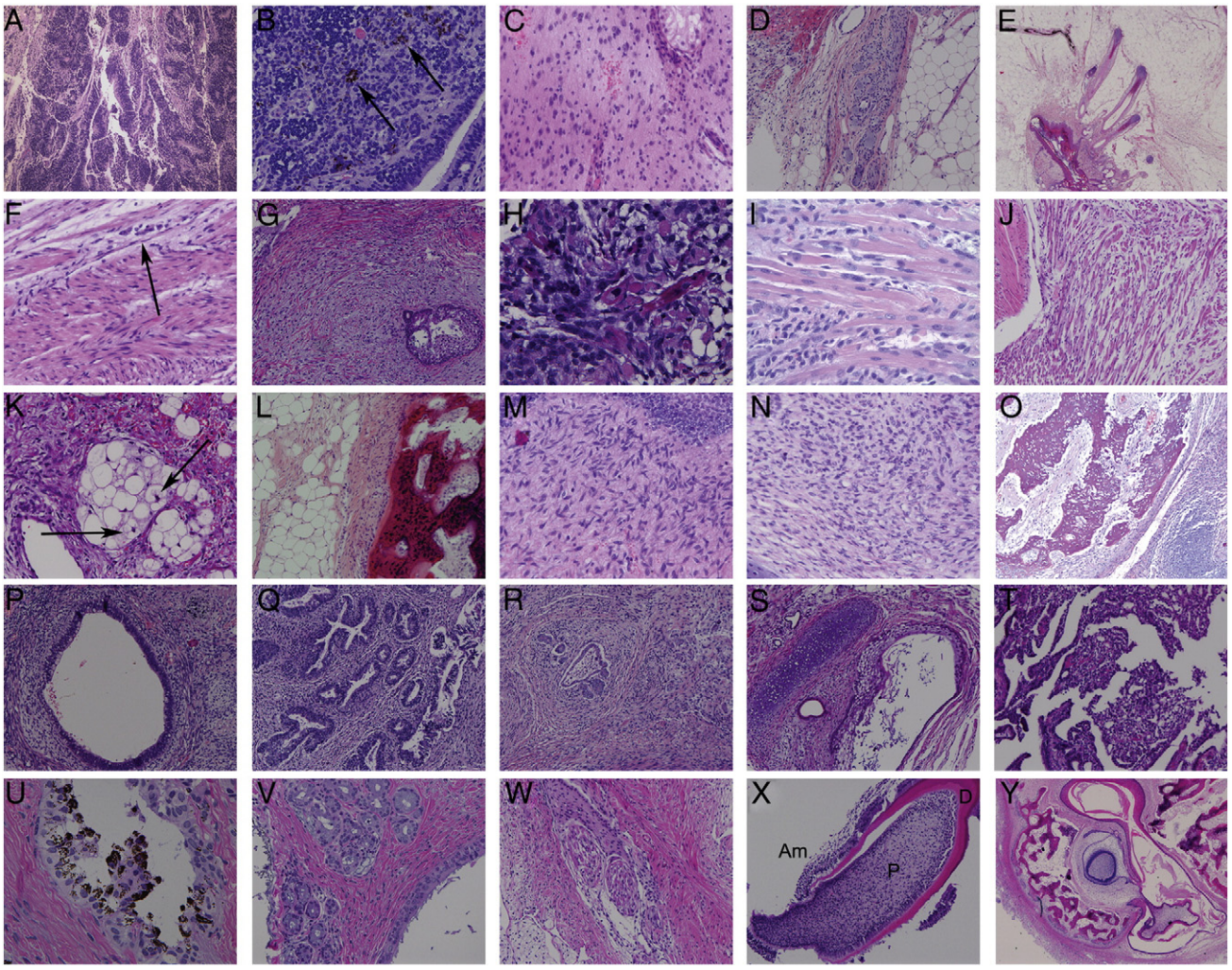

Figure 1 Collage of images of hematoxylin and eosin-stained tissue sections representing the range of tissues present in teratomas from pedigreed nhpESC lines. A–E represent ectodermal derivatives, F–O mesodermal derivatives, P–T endodermal derivatives, and U–Y interesting isolated findings. (A) Neuroepithelium showing stratified epithelium arranged in ribbons and rosettes (40×). (B) Immature neuroglia focus composed of neuroblastic cells (200×). A few pigmented cells within rosettes are present and may represent early retinal anlagen (arrows). (C) Mature neuroglia containing both neurons and glial cells. A remnant of a testicular tubule is present in the upper right (200×). (D) Mature ganglion (100×). (E) Well-developed skin with adnexal structures and hair follicles extending deep into the surrounding adipose tissue (20×). (F) Mature smooth muscle with a developing myenteric plexus containing immature ganglion cells (arrow) (200×). (G) Immature smooth muscle surrounding an immature gland (100×). (H) Immature skeletal muscle showing multinucleated myotubes and rhabdomyoblasts within cellular stroma (400×). (I) Mature skeletal muscle composed of long striated myofibers (400×). (J) Mature skeletal muscle comprising a large area of tissue in the 3106 line (100×). (K) Focus of immature adipose tissue. Note the variably sized individual adipocytes and lipoblasts with centrally located nuclei (arrows) (200×). (L) Mature adipose tissue showing a lobule adjacent to bone (right) (100×). Note the generally uniform size of adipocytes. (M) Cellular immature mesenchyme seen beneath developing epithelium (top right) (200×). The cells have spindle-shape nuclei and scattered mitoses. (N) Fibromuscular stroma (200×). (O) Mature bone without bone marrow (100×). (P) Immature gland surrounded by immature smooth muscle. Some glandular cells show apical clear cytoplasm (100×). (Q) Collection of immature ectactic glands some with a staghorn appearance surrounded by immature smooth muscle/fibromuscular stroma. This collection resembles immature prostate tissue (100×). (R) Isolated immature gland showing a few early epithelial buddings (100×). (S) Immature gland composed of stratified cuboidal epithelium with hint of a basal layer. Note adjacent cartilage (100×). (T) Focus of immature tissue resembling yolk sac. Many of the cells have sub- and supranuclear cytoplasmic clearing (piano keys) (100×). (U) Pigmented cells lining a glandular space (400×). (V) Glands resembling salivary gland near an epithelial structure (duct) (lower right) (200×). (W) Intimately associated nerve and muscle resembling a rare pathological entity seen in young children; neuromuscular hamartoma (100×). (X, Y) Developing tooth seen in 3106. X shows immature tooth organ with central pulp (P) surrounded by dentin layer (D) and ameloblastic epithelium (Am) (100×). (Y) Tooth bell from same teratoma (20×).

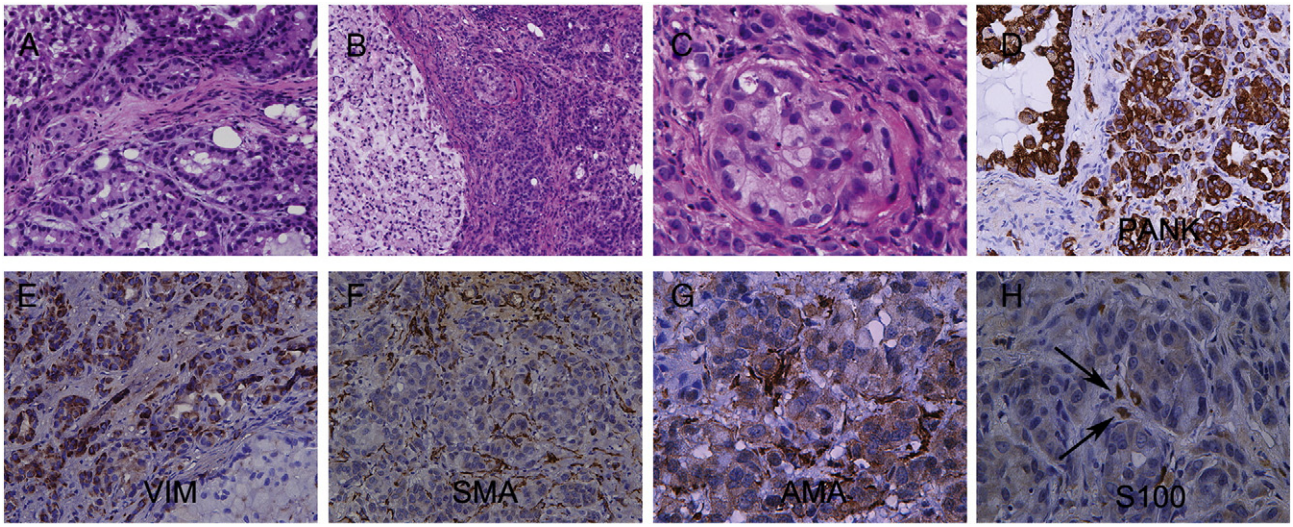

Figure 2 Tumor derived from 106-A1 and A2 lines. A–C are hematoxylin and eosin-stained images of the tumor. In panel A, many areas showed glandular profiles composed of cells with basally oriented nuclei and abundant amphophilic cytoplasm (200×). Focal areas showed cells with a more clear or vacuolated cytoplasm (B) (100×). C shows higher magnification view of glandular profile. Scattered apoptotic debris is present (400×). A selected immunohistochemistry profile is shown in panels D–H. Tumor cells were positive for both cytokeratin and vimentin (D and E, respectively, 200×). Smooth muscle actin and all muscle actin stains highlighted scattered spindle cells interspersed between glandular profiles. Focal light staining of some glandular cells was also seen (F, smooth muscle actin, 200×; G, all muscle actin, 400×). S100 stain (H) showed a rare positive interglandular cell (arrows) (S100; 400×).

et al., 2002; Huisman et al., 2005; Fujimaki et al., 1994). Figure 4 shows a histological section coregistered with a 2D MRM slice. Structures and tissues that could be identified from MRM images with little or no ambiguity were adipose tissue, cyst, cartilage, and epidermal lining. A series of coregistrations similar to that shown in Figure 4 were used to determine which teratoma tissue types and structures were identifiable using MRM. About 30% of attempted slice registrations were successful, while the rest lacked compelling and unambiguous correlation between the two imaging modalities since few landmark features were present in disorganized teratomas. Successful registrations, especially when aided by fiduciary markers (Fig. 5F, see Supplemental Movies for 3D rendering and orthogonal slices), allowed homogeneous tissue patches in histology to be correlated with pixel intensity values in T_2-weighted images. Table 2 shows the results of this series of cross-teratoma correlations. Tissues with low intensity in MR images, defined as 3–22% of maximum (cyst) intensity, included adipose and necrotic tissues, mature bone/cartilage, and neuroectoderm. Tissues with medium intensity (22–52% of maximum intensity) included neuroectoderm, immature bone/cartilage, skin, muscle, connective, gastrointestinal, and necrotic tissues. High-intensity tissues (53–100% of maximum intensity) were limited to cystic lining/fluid and gastrointestinal lining. Notably, because these MR image intensity categories (i.e., low, medium, and high) were found to represent multiple tissue types in histology, MR images were not able to unambiguously label any tissue types except for adipose tissue, cyst, and calcified bone/cartilage. These tissue types were unambiguous due to their texture features. For example, although adipose tissue deposits and mature (calcified) bone/cartilage are both low intensity in MR images, adipose deposits tended to have poorly delineated boundaries, while bone/cartilage exhibited shard-like patterns. High-intensity cysts had bulging shapes with well-delineated linings.

Previously, clinical T_2-weighted MR images also identified adipose tissue as low intensity, cyst as high intensity, and calcification (which increases with bone/cartilage maturity) as low intensity with shard-like textures (Yamaoka et al., 2003; Monteiro et al., 2002; Guo et al., 2007). High-resolution MRM was critical for enabling correlation between MR image intensity with tissue type (Table 2); lower resolution images would not have sufficed. However, these higher resolutions did not allow us to uniquely identify any additional tissue types directly from MR images, when compared with previous clinical imaging. Yet with further analysis, MRM may allow direct, noninvasive identification of additional tissue types, because they revealed textured patterns not visible in low-resolution MRI. For example, in the three teratomas shown in Figure 3, unidentified textures included radial patterns with alternating dark–bright spokes, faint stacks of filamentous parallel lines, dark finger-like projections, faint concentric lines against bright backgrounds, and dark patches with interior textures such as bright speckles or membrane-like lines. Correlating these textures and other regional patterns with the tissues they represent in histology, especially aided by computational statistical methods, could identify additional tissue types with varying levels of confidence, directly from MRM of teratomas.

Discussion

While teratoma assays are crucial for testing pluripotency with stem cells from human and nonhuman primates, their study may provide important insights into development,

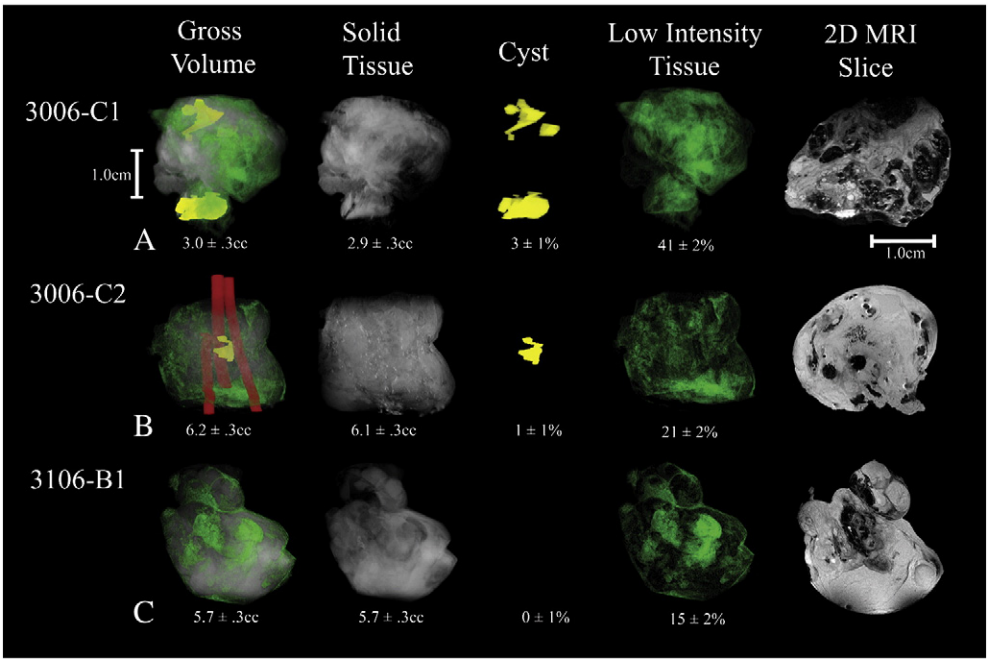

Figure 3 Volumetric teratoma data compiled from 3D MRM segmentation of three teratomas (rows A, B, C). From left to right: Gross Volume represents teratoma volume including cysts and mouse tissues; Solid Tissue (gray) represents teratoma volume after removing cysts and mouse tissues; Cyst (yellow) represents percentage of Gross Volume that is liquid-filled cyst; and Low Intensity Tissue represents the percentage of Solid Tissue that exhibits the lowest 36±7% of MR image intensities after cross-teratoma normalization. The 36% intensity threshold was chosen since tissues below it would tend to have structure and texture (e.g., patches, lines, and punctate spots). The three red cylinders represent toothpicks that were inserted through the volume as fiducial markers to enhance MRM-histological registration and correlation.

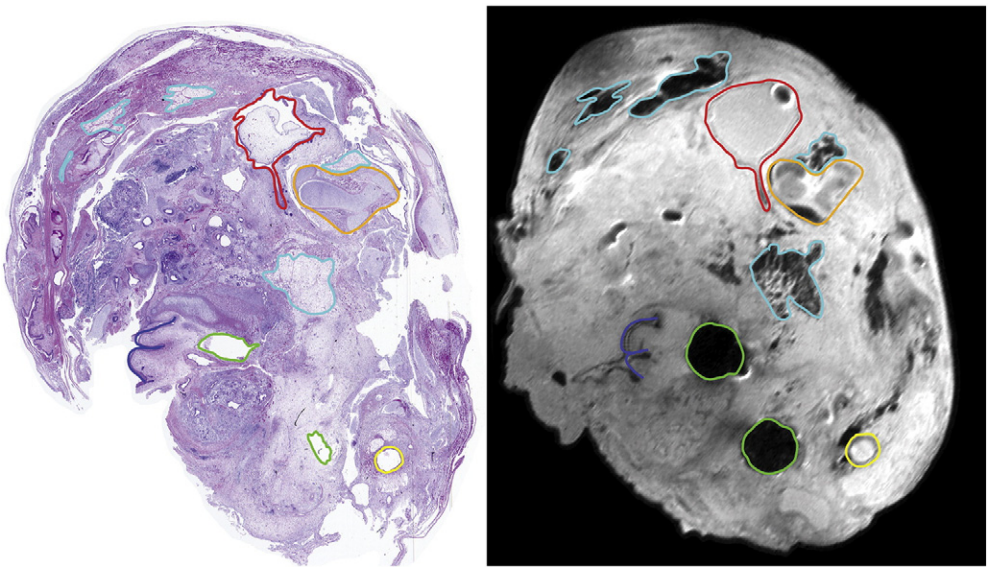

Figure 4 Histological section (left) coregistered with 2D MRM slice (right). Tissues and structures that are clearly differentiated in both histology and MRM are outlined in color. These outlines represent adipose tissue (cyan), cartilage (orange), cystic regions (red, yellow), toothpicks inserted as fiduciary markers (green), and epidermis from skin (blue). Some tissue patches that appear in histology do not appear in MRM because either they do not generate MR contrast or their contrast was diminished due to MR image slice thickness—because the histological section is 5 μm thick, the 180-μm-thick MR image slice represents the sum of 36 histological slices. Finally, some of the tissue that is present in the MR image slice is missing from the histological section, which is an artifact introduced during the sectioning process.

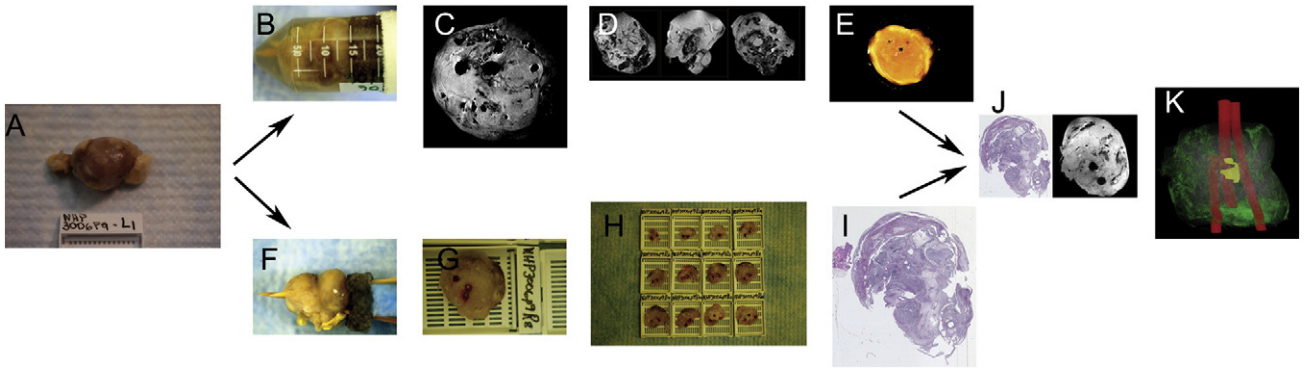

Figure 5 Pipeline for MRM and histopathological analysis of teratomas derived from pedigreed nhpESCs: After isolation (A) and several days of fixation in 10% buffered formalin, wooden fiduciary markers are inserted and the teratoma is placed in a 50-ml conical tube with Fluorinert for MRM imaging (B, F). Representative MR images are shown in panels C, D, and E. G–I show the path for histopathological analysis from cassette to hematoxylin and eosin-stained slide. In this case the teratoma required 12 cassettes for submission of the entire tumor. J represents the alignment of one of the whole slide scanned images to its corresponding MR image. K demonstrates the 3D rendering of the entire teratoma with fiduciary markers in place.

epigenetics, cancer, and tissue regeneration research. Several pluripotent stem cell lines have been derived from nonhuman primate blastocysts and while they have been characterized by their immunocytochemical phenotype, ability to differentiate into multilineage cell phenotypes *in vitro*, and teratomas *in vivo* (some lines) (Mitalipov et al., 2006; Pau and Wolf, 2004), to our knowledge this is the first study that compares and characterizes in a more formal and semiquantitative fashion the morphological landscape of teratomas derived from related families of nhpESCs using histological analysis and MRM.

MRI performed at resolutions <100 μm per 2D voxel has been designated MRM, and is used as a tool for virtual histological studies. Advancements in MRM have increased the resolution at which biological samples are imaged to be as low as 10–16 μm in 2D images and 20–50 μm in 3D volume acquisitions (Tyszka et al., 2005). Many different "virtual tissue stains" can be imparted on MR histology sections by selecting imaging parameters that take advantage of MR contrast mechanisms (Johnson et al., 1993). MR histology is practical for creating large 3D databases that noninvasively depict embryonic development along with anatomical structure annotation (Petiet et al., 2008).

Table 2 Regional correlation of teratoma tissue types with T_2-weighted MRI image pixel intensities

MRI image region intensity	Tissue types found
Low intensity (3–22% of maximum)	Adipose
	Necrosis
	Mature bone
	Mature cartilage
	Neuroectoderm
Medium intensity (22–52% of maximum)	Neuroectoderm
	Immature cartilage
	Immature bone
	Skin
	Skeletal muscle
	Smooth muscle
	Gastrointestinal
	Connective
	Necrosis
High intensity (52–100% of maximum)	Cystic lining
	Respiratory cysts
	Gastrointestinal

MRI has been used to evaluate teratoma prognosis in both adult and prenatal scans (Mazouni et al., 2003). Cysts appear bright and well defined in T_2-weighted MR images (Yamaoka et al., 2003; Monteiro et al., 2002), and fat deposits are also reliably identifiable (Monteiro et al., 2002; Guo et al., 2007). Because cysts are well defined, they have been used to categorize teratomas based on different scales that qualify their cystic fraction—from entirely cystic to solid type (Yamaoka et al., 2003; Danzer et al., 2006). Immature or malignant teratomas tend to have fewer and smaller cystic and calcification components (Fujimaki et al., 1994). Calcifications frequently present as low-intensity punctate, shard-like, or linear high-density strands (Guo et al., 2007). In MR images, solid portions of teratomas exhibit heterogeneous contrast in both T_1-weighted and T_2-weighted MR images (Yamaoka et al., 2003; Huisman et al., 2005; Fujimaki et al., 1994). MRI was found to be superior to sonography for determining the extent of echogenic solid-type teratomas, their content, and their compressive effects on organs (Danzer et al., 2006).

The volumetric teratoma data obtained by MRM was found to have both advantages and disadvantages compared to histology. MRM can deliver accurate volumetric measurements because true 3D images are obtained, and the sample is unaltered by histological processing. With histological sectioning, tissue is discarded, and consequently volume information is discarded as well. Both MRM and histological analysis methods have the potential to introduce artifacts, but in our study neither MRM nor histological artifacts prevented comparison and identification of structures. Histology offers more detail than MR microscopy, but once sectioning is done, 3D volumetric information is lost. Advantages of volumetric data include the ability to section in any plane desired, perform 3D measurements, and quantify accurate tissue fractions, such as for cyst, which has been used to classify teratomas in the clinic (Yamaoka

et al., 2003; Danzer et al., 2006). These advantages allow for focusing on the same tissue target using different perspectives and landmarks. Additionally, many of the artifacts that are potentially introduced by histology can be avoided with MRM, such as tissue shrinkage, wrinkles, and other cutting deformities. MRM introduced some artifacts; most notably fluid-filled channels such as intestinal lining showed up dark, instead of bright in images. This is likely caused by the difference in magnetic susceptibility between the fluid and its adjacent tissue, causing loss of signal in T_2-weighted images. T_1-weighted images were also tested, but were found to generate unsatisfactory levels of contrast between tissues, given image quality and signal-to-noise levels. However, T_1 weighting did appear to generate different contrasting effects for tissues compared to T_2 weighting, so it may be useful in future studies as an additional "virtual tissue stain."

Image registration between MRM and histology required vigilant sample alignment, but allowed for correlation between MR image intensity values and histological tissue types. At a high MRM voxel resolution of $100 \times 50\ \mu m$, only calcified, adipose, and cystic tissues were identifiable based on MR intensity values and tissue textures—other tissue types shared similar intensity values and textures, and therefore were not able to be confidently identified. When compared to relatively low-resolution clinical MRM scans, no additional tissue types were identifiable when using MRM. Computational textural and shape analysis trained over many teratomas, as well as higher resolutions, may offer improved tissue identification by better resolving and considering textures.

Careful microscopic inspection of each block of serially sectioned teratoma tumors processed by routine histological methods revealed a wide range of tissue types whose origins derive from one of the three germ layers. We identified the majority of tissue types from the H&E slides without the need for ancillary studies. We emphasize two critical aspects of the histopathological analysis that allow for optimal examination of teratomas. One, we underscore the importance of having well-processed and well-stained H&E sections. Well-processed tissue includes having the entire teratoma well fixed (several days), serially sectioned at 2–3 mm, and processed so that it is free of tissue drying and microtome cutting artifacts. This is particularly important since generally speaking, these tumors are large, thus generating a tissue section with a large cross-sectional area compared to a small tissue biopsy. We recommend using a regressive H&E stain as outlined in Supplemental Document 1. We believe that this achieves greater nuclear detail and less interference from staining of cytoplasmic nucleic acids. Two, it is essential to have a versatile and experienced pathologist examine all of the tissue sections of the tumor carefully. The pathologist should be comfortable with the microscopic examination of a wide variety of organ systems including perinatal and/or pediatric specimens and experienced in identifying seemingly inconsequential structures within the milieu of tissues present. Perinatal and/or pediatric clinical pathology disciplines tend to have specimens that include fetal organs, organs with developmental arrest/neoplasia, extraembryonic tissues, and clinical teratomas. We were able to semiquantify each tissue type to show similarities and differences in germ layer composition and correlate some specific tissue types with MRM.

There are some limitations in this study. One is the semiquantification of the tissue types and in related fashion semiquantification in two dimensions. The process of semiquantification of these relatively few teratomas was a time-consuming and ultimately imprecise process, hence the estimations of percentage ranges used for scoring each representative slide from each block of teratoma. By its nature the teratoma is a complex amalgamation of tissue types that are in close approximation to one another often without distinct boundaries. For example, areas of striated muscle (immature and mature) could be seen intermingled with the bland but prevalent mesenchymal stroma, making exact quantification of these two distinct tissues very difficult unless present uniformly over a reasonably large microscopic area. Quantification of tissue types and structures in three dimensions would add additional important information, most notably, the relationships of tissue and developing organs to one another. To these ends, the ability to automatically identify and segment specific tissue types and reconstruct them in three dimensions by computerized means would greatly advance this area of developmental biology. Recently, our group and others have made advances in the application of algorithms and techniques used in automated image analysis specifically applied to recognition of tissue types in teratomas (Oh et al., 2009; Chebira et al., 2008). The use of numerous immunohistochemical markers would aid quantitative analysis of specific tissue types (and hence germ layer derivation), although we suspect that some tissues, particularly more undifferentiated and primitive tissues, may not have commercially available antibodies that would both perform adequately in formalin-fixed paraffin-embedded tissues and also elucidate specific phenotypes. Even with commercially available antibodies some tissues (i.e., immature neuroglial tissue) did not stain uniformly with neuroblastic markers (e.g., PGP9.5; not shown), reflecting their phenotypic diversity.

In summary, MRM of teratomas likely yields useful information when studying certain tissue type development (i.e., fat or bone) and overall growth characteristics of the teratoma. Teratomas, overall, demonstrate a striking variety of tissue types derived from the three germ layers. Teratomas derived from pedigreed nonhuman primate embryonic stem cells may be a useful model for comparing tissue composition in teratomas derived from ESCs of related families as well as for studying skin, bone, adipose, and intestinal development in light of the histopathological and MRM findings. As techniques improve in MRM and image analysis, more tissue derivatives will be able to be identified using noninvasive means. The MRM platform will allow for longitudinal study of teratoma development *in vivo* perhaps using labeled ESCs capable of being tracked by MRM. The techniques and analysis presented provide for a rigorous and standardized approach for examination and reporting of teratomas derived from embryonic stem cells.

Methods

Teratoma formation

Stem cells have been derived as described previously by Navara et al. (2007). For this study we used a number of

pedigreed ES lines divided into two families (Supplemental Fig. 1). A family of ES lines was derived simultaneously from the same sperm donor and the same clutch of prime quality eggs. Stem cell pluripotency potentials are assessed by teratoma formation in SCID mice as follows: Nonhuman primate ESCs were isolated by scraping colonies with good morphology followed by a brief 5 min treatment with 0.25% trypsin/EDTA to break up large fragments. Cells were pelleted at 200 *g* for 5 min, washed twice in sterile PBS, and approximately 5×10^5–5×10^6 cells were injected into the testis of 8- to 12-week-old NOD-SCID mice (The Jackson Laboratory, Bar Harbor, ME) by modification of efferent duct injection (Ogawa et al., 1997). The injection pipette was advanced along the efferent duct and through the rete testes into the interstitial space where cells were injected (using Eppendorf Femtojet). The injection itself was monitored with trypan blue added to the cell suspension. Tumor growth was determined by palpation and was typically detectable by 10–12 weeks after injection. Mice were euthanized when tumors became too bulky or impaired the ability of the animal to ambulate, eat, or drink in a normal fashion according to Institutional Animal Care and Use Committee guidelines. In all, we injected 34 mice from which we generated 27 teratomas for analysis. The overall outline of our experiments is depicted in Figure 5. Teratomas were extracted from mice as described (Fig. 5A) and used for MRM examination (Figs. 5B–E) and/or histopathological examination (Figs. 5F–I). These results were used to compare histopathology with MRM (Fig. 5J) and produce a 3-D model in MRM (Fig. 5K).

Magnetic resonance microscopy

After fixation in 10% phosphate-buffered formalin for a minimum of 5–7 days at room temperature, teratomas were immersed in liquid Fluorinert (3M Corporation, St. Paul, MN) and sealed in a plastic conical tube with the smallest reasonable radius so that MR signal from the tissue sample is maximized (Fig. 5B). Fluorinert has no proton MRM signal, facilitating 3D surface renderings and volume analysis. One teratoma had three wooden (i.e., low magnetic susceptibility) fiduciary markers inserted at different angles to aid later attempts at coregistration between MR and histological images. The teratoma samples were then imaged using a 30 mm diameter, birdcage radiofrequency resonator in an 89-mm vertical-bore 11.7T Bruker AVANCE imaging system (Bruker BioSpin Corporation, Billerica, MA). The sample temperature was cooled and regulated at 12 °C, increasing MR signal by ~4%. Image data were acquired using a T_2-weighted multislice spin-echo pulse sequence with parameters as follows: matrix size 512×256, TE/TR=50/2000 ms, averages=24, and slice thickness=1.0 mm. Additionally, 3D scans were acquired using a T_2-weighted spin-echo pulse sequence with parameters as follows: matrix size 512×256×128, TE/TR=50/2000 ms, averages=3, and voxel size=50 μm×100 μm×180 μm. The spin-echo pulse sequence was chosen to avoid T_2^* magnetic field inhomogeneity artifacts, which can be prominent at high field strengths like 11.7 T. The TR=2000 ms value was chosen to ensure full longitudinal magnetization recovery and generate images with pure T_2 weighting. The optimal TE value of 50 ms was empirically determined by performing scans across a range of TE values, finding the value that maximized image contrast between different teratoma tissue types, while also remaining short enough to retain satisfactory MR image quality (i.e., signal-to-noise ratio). T_1-weighted images were also tested, but were found to generate unsatisfactory levels of contrast between tissues.

MRM 3D volume rendering, volume statistics, and histological correlation

All acquired teratoma MRM datasets were zero-filled to form isotropic voxels, to facilitate rendering and volume measurements. Volume data were imported into the 3D rendering software Amira (Mercury Computer Systems, Chelmsford, MA). The program was used to segment each teratoma into its cystic, solid tissue, and low-intensity tissue components. Low-intensity tissue represents the percentage of solid tissue that exhibits the lowest 36±7% of MRM image intensities after cross-teratoma normalization to cystic fluid, which was found to be similarly composed across all three samples. The 36% intensity threshold was chosen since tissues below it would tend to have structure and texture (e.g., patches, lines, and punctate spots). The software was also used to create histogram profiles of the teratoma, compute volumetric quantities for each segmented tissue type, and render 3D visualizations.

MRM datasets were correlated with histology to determine what tissue types and structures were identifiable using MR microscopy. A series of histological slices that featured homogeneous patches of different tissue types were manually registered with MRM datasets. For each slice that could be successfully registered between MRM and histology, each homogeneous patch of tissue in histology was located in MR images, and vice versa, in order to record correlations between tissue type and T_2-weighted image intensity values. To reduce potential error, at least three occurrences of each tissue type were identified in order to generate correlations.

Tissue processing and imaging

Teratomas were fixed in 10% phosphate-buffered formalin for at least 5–7 days (depending on the size of the tumor and prior to sectioning or MRM scan) and sectioned at approximately 3-mm intervals using Thomas tissue slicer blades (Thomas Scientific, Inc., Swedesboro, NJ) perpendicular to the orientation of the teratoma within the conical tube used for MRM. The tumor was sectioned from left to right and sections were kept in orientation with respect to neighboring sections (left cut face kept next to right cut face). Sections were placed face down and kept in the same orientation with respect to each other into labeled tissue cassettes and processed on a conventional graded-alcohol tissue processor (Tissue-Tek VIP 5, Sakura Finetek USA, Inc., Torrance, CA) (see Supplemental Document 1 for processing protocol) and paraffin-embedded maintaining the same orientation as when initially sectioned. A representative 5-μm section from each block was obtained using a microtome (Shandon Finesse 325, Thermo Fisher Scientific, Inc., Waltham, MA), floated out on a 40 °C water bath and picked up using Superfrost Plus slides (Fisher Scientific Inc., Hampton, NH).

Sections were air-dried for 5–10 min and placed overnight in a 60 °C oven and then stained using a regressive hematoxylin and eosin (H&E) staining procedure (see Supplemental Document 2 for staining protocol). Tumors were examined microscopically by pathologists (J.A.O. and C.A.C.) and designated as a teratoma if tissue representation from all three germ layers was identified microscopically (see Supplemental Table 2 for tissue derivatives from respective germ layers). All images in this study were acquired using an Olympus BX51 microscope equipped with UIS2 objectives (Olympus America, Inc., Central Valley, PA) and 2-mega pixel SPOT Insight camera (Diagnostic Instruments Inc., Sterling Heights, MI) or Nikon 90i microscope equipped with a DS-Ri1 12 million pixel shifting camera (Nikon Instruments, Inc., Melville, NY).

Semiquantitative scoring of tissues derived from germ layers

All histological sections of teratomas and lesions derived from injections of nhpESCs derived from these two families were reviewed by pathologists (J.A.O., C.A.C.). For those tumors designated as teratomas, tissue derived from each of the germ layers was semiquantitated by examining the representative section from each block of the entirely sectioned teratoma. Tissue types were identified and categorized as belonging to ectoderm, mesoderm, or endoderm and the percentage of the area of the slide occupied by each tissue type was estimated according to the following key: 0, no tissue present; 1, 1–20%; 2, 21–40%; 3, 41–60%; 4, 61–80%; and 5, 81–100%. The median of the percentage range was then taken for all blocks for each tissue type. For each germ layer, the medians representing the percentage range of the tissue types derived from that germ layer were summed and an overall percentage range was assigned to that germ layer.

Immunohistochemistry

Immunohistochemical analyses were performed on the formalin-fixed, paraffin-embedded tissue sections from the tumor derived from the 106-A1/A2 lines. Primary antibodies were directed against the following antigens: pancytokeratin (epithelial marker; ectoderm) (mouse monoclonal, predilute, Ventana Medical Systems, Tucson, AZ), smooth muscle actin (mesoderm) (mouse monoclonal, 1:250, Dako Corporation, Carpinteria, CA), S100 (rabbit polyclonal, 1:100, Vector Laboratories Inc., Burlingame, CA), vimentin (mesoderm) (mouse monoclonal, predilute, Ventana), all muscle actin (mesoderm) (clone HHF35, mouse monoclonal, predilute, Ventana), PGP9.5 (ectoderm) (neuroendocrine/neuroblast marker, mouse monoclonal, 1:25, Vector), myogenin (rhabdomyosarcoma marker, mouse monoclonal, 1:500, Dako), alpha-fetoprotein (endoderm) (rabbit polyclonal, 1:1000, Dako), Oct3/4 (pluripotency marker) (rabbit polyclonal, predilute, Biocare Medical), and p63 (epithelial progenitor/stem cell and basal cell marker)(mouse monoclonal, clone 4A4, 1:200, LabVision). All immunohistochemical staining was performed using appropriate antigen retrieval on a Ventana Benchmark XT automated stainer (Ventana Medical Systems, Tucson, AZ) (with the exception of Oct3/4 and p63) according to standardized protocols. A standard avidin–biotin complex technique was used for detection.

Supplementary materials related to this article can be found online at doi:10.1016/j.scr.2010.07.005.

Acknowledgments

This work was supported by NIH Grant 3P01HD047675-05S1. The authors gratefully appreciate the work of Clifford Smay, HT (ASCP) in the Histology Core Facility at Magee Womens Research Institute, and Lori Schmitt in the Pathology Laboratory at Children's Hospital of Pittsburgh for providing the tissue sections and immunohistochemistry presented in this paper.

References

Aleckovic, M., Simon, C., 2008. Is teratoma formation in stem cell research a characterization tool or a window to developmental biology? Reprod. Biomed. Online 17, 270–280.

Cao, F., Li, Z., Lee, A., Liu, Z., Chen, K., Wang, H., Cai, W., Chen, X., Wu, J.C., 2009. Noninvasive de novo imaging of human embryonic stem cell-derived teratoma formation. Cancer Res. 69, 2709–2713.

Chebira, A., Ozolek, J.A., Castro, C.A., Jenkinson, W.G., Gore, M., Bhagavatula, R., Khaimovich, I., Ormon, S.E., Navara, C.S., Sukhwani, M., Orwig, K.E., Ben-Yehudah, A., Schatten, G., Rohde, G.K., Kovacevic, J., 2008. Multiresolution identification of germ layer components in teratomas derived from human and nonhuman primate embryonic stem cells. Proc. IEEE Int. Symp. Biomed. Imaging 979–982.

Damjanov, I., 1993. Teratocarcinoma: neoplastic lessons about normal embryogenesis. Int. J. Dev. Biol. 37, 39–46.

Danzer, E., Hubbard, A.M., Hedrick, H.L., Johnson, M.P., Wilson, R.D., Howell, L.J., Flake, A.W., Adzick, N.S., 2006. Diagnosis and characterization of fetal sacrococcygeal teratoma with prenatal MRI. AJR Am. J. Roentgenol. 187, W350–W356.

Fujimaki, T., Matsutani, M., Funada, N., Kirino, T., Takakura, K., Nakamura, O., Tamura, A., Sano, K., 1994. CT and MRI features of intracranial germ cell tumors. J. Neurooncol. 19, 217–226.

Guo, Y.K., Yang, Z.G., Li, Y., Deng, Y.P., Ma, E.S., Min, P.Q., Zhang, X.C., 2007. Uncommon adrenal masses: CT and MRI features with histopathologic correlation. Eur. J. Radiol. 62, 359–370.

Huisman, T.A., Fischer, U., Boltshauser, E., Straube, T., Gysin, C., 2005. Pituitary duplication and nasopharyngeal teratoma in a newborn: CT, MRI, US and correlative histopathological findings. Neuroradiology 47, 558–561.

Hyun, I., Lindvall, O., Ahrlund-Richter, L., Cattaneo, E., Cavazzana-Calvo, M., Cossu, G., De Luca, M., Fox, I.J., Gerstle, C., Goldstein, R.A., Hermeren, G., High, K.A., Kim, H.O., Lee, H.P., Levy-Lahad, E., Li, L., Lo, B., Marshak, D.R., McNab, A., Munsie, M., Nakauchi, H., Rao, M., Rooke, H.M., Valles, C.S., Srivastava, A., Sugarman, J., Taylor, P.L., Veiga, A., Wong, A.L., Zoloth, L., Daley, G.Q., 2008. New ISSCR guidelines underscore major principles for responsible translational stem cell research. Cell Stem Cell 3, 607–609.

Johnson, G.A., Benveniste, H., Black, R.D., Hedlund, L.W., Maronpot, R.R., Smith, B.R., 1993. Histology by magnetic resonance microscopy. Magn. Reson. Q. 9, 1–30.

Lanza, R.P., 2006. Essentials of Stem Cell Biology. Elsevier/Academic Press, Amsterdam.

Lehman, J.M., 1980. Studies of teratomas in mice: possibilities for the future production of animal models. Am. J. Pathol. 101, S33–S40.

Lehtonen, E., Laasonen, A., Tienari, J., 1989. Teratocarcinoma stem cells as a model for differentiation in the mouse embryo. Int. J. Dev. Biol. 33, 105–115.

Mazouni, C., Porcu-Buisson, G., Girard, N., Sakr, R., Figarella-Ballanger, D., Guidicelli, B., Bonnier, P., Gamerre, M., 2003. Intrauterine brain teratoma: a case report of imaging (US, MRI) with neuropathologic correlations. Prenat. Diagn. 23, 104–107.

Mitalipov, S., Kuo, H.C., Byrne, J., Clepper, L., Meisner, L., Johnson, J., Zeier, R., Wolf, D., 2006. Isolation and characterization of novel rhesus monkey embryonic stem cell lines. Stem Cells 24, 2177–2186.

Monteiro, M., Cunha, T.M., Catarino, A., Tome, V., 2002. Case report: sacrococcygeal teratoma with malignant transformation in an adult female: CT and MRI findings. Br. J. Radiol. 75, 620–623.

Mountford, J.C., 2008. Human embryonic stem cells: origins, characteristics and potential for regenerative therapy. Transfus. Med. 18, 1–12.

Muller, F.J., Goldmann, J., Loser, P., Loring, J.F., 2010. A call to standardize teratoma assays used to define human pluripotent cell lines. Cell Stem Cell 6, 412–414.

Navara, C.S., Mich-Basso, J.D., Redinger, C.J., Ben-Yehudah, A., Jacoby, E., Kovkarova-Naumovski, E., Sukhwani, M., Orwig, K., Kaminski, N., Castro, C.A., Simerly, C.R., Schatten, G., 2007. Pedigreed primate embryonic stem cells express homogeneous familial gene profiles. Stem Cells 25, 2695–2704.

Ogawa, T., Arechaga, J.M., Avarbock, M.R., Brinster, R.L., 1997. Transplantation of testis germinal cells into mouse seminiferous tubules. Int. J. Dev. Biol. 41, 111–122.

Oh, S.K., Chua, P., Foon, K.L., Ng, E., Chin, A., Choo, A.B., Srinivasan, R., 2009. Quantitative identification of teratoma tissues formed by human embryonic stem cells with TeratomEye. Biotechnol. Lett. 31, 653–658.

Pau, K.Y., Wolf, D.P., 2004. Derivation and characterization of monkey embryonic stem cells. Reprod. Biol. Endocrinol. 2, 41.

Petiet, A.E., Kaufman, M.H., Goddeeris, M.M., Brandenburg, J., Elmore, S.A., Johnson, G.A., 2008. High-resolution magnetic resonance histology of the embryonic and neonatal mouse: a 4D atlas and morphologic database. Proc. Natl. Acad. Sci. USA 105, 12331–12336.

Prelle, K., Zink, N., Wolf, E., 2002. Pluripotent stem cells—model of embryonic development, tool for gene targeting, and basis of cell therapy. Anat. Histol. Embryol. 31, 169–186.

Sternberg, S.S., 1989. Diagnostic Surgical Pathology. Raven Press, New York.

Tyszka, J.M., Fraser, S.E., Jacobs, R.E., 2005. Magnetic resonance microscopy: recent advances and applications. Curr. Opin. Biotechnol. 16, 93–99.

Yamaoka, T., Togashi, K., Koyama, T., Fujiwara, T., Higuchi, T., Iwasa, Y., Fujii, S., Konishi, J., 2003. Immature teratoma of the ovary: correlation of MR imaging and pathologic findings. Eur. Radiol. 13, 313–319.